Entrainment-zone restratification and flow structures in stratified shear turbulence

By B. Anders Pettersson Reif †, Joseph Werne ‡, Øyvind Andreassen†, Christian Meyer ‡, AND Melissa Davis-Mansour‡

Late-time dynamics and morphology of a stratified turbulent shear layer are examined using 1) Reynolds-stress and heat-flux budgets, 2) the single-point structure tensors introduced by Kassinos *et al.* (2001), and 3) flow visualization via 3D volume rendering. Flux reversal is observed during restratification in the edges of the turbulent layer. We present a first attempt to quantify the turbulence-mean-flow interaction and to characterize the predominant flow structures. Future work will extend this analysis to earlier times and different values of the Reynolds and Richardson numbers.

1. Introduction

Stable density stratification poses several significant challenges for turbulence modeling. Unlike the case of unstable stratification (for which numerous potential turbulence nucleation sites may trigger volume-filling motion), turbulence in stable stratification must satisfy more difficult onset conditions, and once initiated, must combat the damping effects of the background density gradient, which acts to confine the turbulence in the vertical direction and eventually to suppress it.

There are two primary mechanisms by which naturally-occurring turbulent motion may be initiated in stably-stratified fluids: 1) shear instability and 2) internal gravity-wave breaking. In both cases conditions for onset are satisfied by wind-driven forcing, either such that a) local Richardson-number criteria are met or b) propagating waves are generated which travel into regions of favorable shear or density variation for overturning. Once overturning and the consequent turbulent mixing occurs and subsides, the resulting background velocity and density profiles are left in a restratified state that is only marginally unstable, optimally configured to act as a nucleation site for the next turbulence-instigating event, even if that event does not occur for a significant period of time.

The challenge for modeling turbulence in stable environments is that the confinement in the vertical direction is often severe (e.g., a few hundred meters in the troposphere and stratosphere and only tens of meters in the ocean thermocline); hence the entire process (i.e., not just the smallest scales) can be sub-grid in scale. Nevertheless, the impact on mixing and mean flows can be significant, and because the restratified layer is marginally unstable and will therefore probably become unstable again at some time in the future, potential subgrid-scale (SGS) temporal coherence over very long periods of time is possible. Even more challenging is the characterization of SGS wave transport processes and distant overturning (possibly in remote restratification zones), implying the necessity for non-local SGS descriptions of wave dynamics and transport and coupling to restratified layers which will likely also be sub-grid in scale.

† Norwegian Defence Research Establishment (NDRE)
‡ Colorado Research Associates Div., Boulder, CO, NorthWest Research Associates, Inc.

In this report we examine some of the aspects of restratification in a turbulent mixing layer generated by the Kelvin-Helmholtz (KH) instability. Because restratification occurs first in the edges of the layer, much of our interest during this initial effort is focused on the dynamics in the layer edges and in comparisons between the edges and the middle of the layer. Our near-term goals are to characterize the dynamics of the fluctuating fields and the flow structures during restratification, and to examine the ramifications for modeling. To this end, we begin by making a detailed exploration of the budgets for the Reynolds stress and heat flux and by exploring the potential of the single-point structure tensors introduced by Kassinos *et al.* (2001) for describing the flow features and morphology. If this latter effort is successful, we anticipate these structure tensors may 1) provide a means to characterize the energy-containing structures and 2) be a valuable component in future modeling efforts. More work is necessary to expand on the work we begin here.

2. Numerical simulations

2.1. *Problem formulation*

To simulate the non-linear evolution of the Kelvin-Helmholtz instability and subsequent turbulence dynamics, we begin with the Boussinesq approximation in a Cartesian geometry. A streamwise background flow $u = U_o \tanh(z/h)$ is initiated with constant velocity U_o and length scale h; z is the vertical dimension. The background temperature is initially linear: $T = \beta z$, where β is the constant mean gradient.

The equations of motion describing momentum, heat, and mass conservation are

$$\partial_t \vec{u} + \vec{\omega} \times \vec{u} = Re^{-1} \nabla^2 \vec{u} - \vec{\nabla} \left(P + \vec{u} \cdot \vec{u} \,/\, 2 \right) + \vec{Ri}\, T \ , \tag{2.1}$$

$$\partial_t T + \vec{u} \cdot \vec{\nabla} T = Pe^{-1} \nabla^2 T \ , \text{ and} \tag{2.2}$$

$$\vec{\nabla} \cdot \vec{u} = 0 \ . \tag{2.3}$$

Here $\vec{u} = (u, v, w)$ and $\vec{x} = (x, y, z)$ are velocity and position vectors; $\vec{\omega} = \vec{\nabla} \times \vec{u}$. All quantities are non-dimensional, using characteristic time h/U_o, length h, velocity U_o, and temperature βh scales. The non-dimensional parameters $Ri = N^2 / \max(\partial_z u)^2$, $Re = U_o h/\nu$, and $Pe = U_o h/\kappa$ are the Richardson, Reynolds, and Peclet numbers, and $\vec{Ri} = Ri\ \hat{z}$. $N^2 = g\alpha\beta$ is the square of the buoyancy frequency, and ν and κ are the kinematic viscosity and thermal diffusivity. g and α are the acceleration due to gravity and the thermal expansion coefficient, respectively. $Ri = 0.05$ and $Re = Pe = 2500$ are used for the 3D solutions presented below. Equality of Re and Pe implies $Pr = \nu/\kappa = 1$, which is near the value for air ($Pr_{air} \approx 0.7$), while $Ri < 0.25$ indicates dynamic instability (Miles (1960)).

To obtain numerical solutions we proceed as follows. First, the solenoidal condition (2.3) is satisfied exactly by employing a two-streamfunction decomposition:

$$\vec{u} \ = \ \vec{\nabla} \times \vec{\psi} \ + \ \vec{\nabla} \times \vec{\nabla} \times \vec{\phi} \ + \ \vec{U}(z) \ . \tag{2.4}$$

Here $\vec{\psi}$ and $\vec{\phi}$ are given by $\vec{\psi} = \psi \hat{z}$ and $\vec{\phi} = \phi \hat{z}$. $\vec{U}(z)$ refers to the mean velocity in the x and y directions (the mean vertical velocity $U_3(z)$ is identically zero).

We numerically integrate evolution equations for the scalar fields ψ, ϕ, and θ, which we obtain by 1) substituting $T = z + \theta$ into (2.2) and by 2) retaining the vertical components of the equations that result when the operators $\vec{\nabla} \times$ and $\vec{\nabla} \times \vec{\nabla} \times$ are applied to (2.1). Note that this eliminates the pressure from the system of equations, since $\vec{\nabla} \times \vec{\nabla} P \equiv 0$.

The boundary conditions are periodic in the horizontal directions, and stress-free with fixed-temperature on the top and bottom boundaries. Solutions are obtained with a pseudo-spectral Galerkin algorithm, with field variables represented horizontally by Fourier series and vertically by either sine or cosine expansions. Nonlinear terms are evaluated in physical space, while differentiation operations and time advancement are carried out in spectral space. Linear terms are treated implicitly, while nonlinear terms are handled explicitly, using the mixed implicit/explicit third-order Runge-Kutta scheme developed by Spalart *et al.* (1991) with a CFL number of 0.68.

We initiate the motion with the most-rapidly-growing asymptotic linear eigenmode ($\lambda \approx 4\pi$) with a Kolmogorov noise spectrum added to the velocity field. Vorticity amplitudes for these perturbations are 0.07 and 0.014, respectively. To accommodate the eigenmode and the anticipated "secondary instability" (Klaassen & Peltier (1985), Klaassen & Peltier (1991), Palmer *et al.* (1994), Smyth & Moum (2000a), Smyth & Moum (2000b)), horizontal dimensions of $x_o \times y_o = 12.56 \times 4.2$ are used. Sufficient remoteness of top and bottom boundaries is established with 2D tests, and $z_o = 25$ is chosen.

Spatial resolution (i.e., number of spectral modes) is varied during the evolution so that small-scale features are always properly represented; this includes thermal and viscous dissipation scales. With $Re = 2500$, as many as $1200 \times 400 \times 2400$ modes are required.

2.2. *Basic flow evolution*

Plate 1 shows the flow morphology with $Re = 2500$. The lower left panel shows the dissipation fields at $t = 77$ when the primary Kelvin vortex is well formed. At this time the depth of the mixing layer (at its deepest) is roughly $6h$, and the velocity difference is $2U_o$, so the layer Reynolds number is $Re_L \approx 30,000$. The initially-stable density stratification is inverted by the primary vortex so that the flow becomes unstable in the vortex-edge regions, and secondary rolls aligned with the streamwise direction develop (Klaassen & Peltier (1985), Klaassen & Peltier (1991), Palmer *et al.* (1994), Smyth & Moum (2000a), Smyth & Moum (2000b)). These secondary rolls are evident in the view from above (middle left panel), which shows tongues of intense thermal gradients in upflow regions at the edge of the mixing layer, interleaved with downflow regions with reduced thermal gradients. The top left panel clearly shows the secondary rolls, using the vortex visualization technique of Jeong & Hussain (1995). The center and right panels show the evolution of the flow at later times, when the vortex tubes interact and trigger the development of small-scale turbulence (Fritts *et al.* (1998)). Note that despite the reflection symmetry of (2.1)-(2.3), e.g., $(\vec{x}, \vec{u}, T) \rightarrow -(\vec{x}, \vec{u}, T)$, asymmetries in flow perturbations can produce apparent spontaneous symmetry breaking in the solutions (e.g., note differences in the upper and lower edges in the lower right panel).

Figure 1 shows the total kinetic energy KE and maximum vorticity for the velocity field with the horizontal mean removed. Oscillations in KE reveal interactions between the primary billow and the horizontal mean. Fluctuations in the vorticity maxima indicate the turbulence intensity of the small scales of motion (Werne & Fritts (1999)).

For the study presented here, we examine the turbulence budgets and statistics during the turbulence-decay phase of the flow evolution ($t > 175$) when the mean fields undergo restratification. Figure 2 shows mean profiles for streamwise velocity and temperature for $t = 240$, i.e. well into the turbulence-decay phase. We can see from the figure that mixing in the interior of the layer has homogenized the velocity and temperature fields there, compressing the initial mean gradients into the edge regions. Despite the enhanced shear that results in the edge of the layer, the combined action of shear and temperature-gradient increase results in a larger Richardson number in the edge of the layer than in

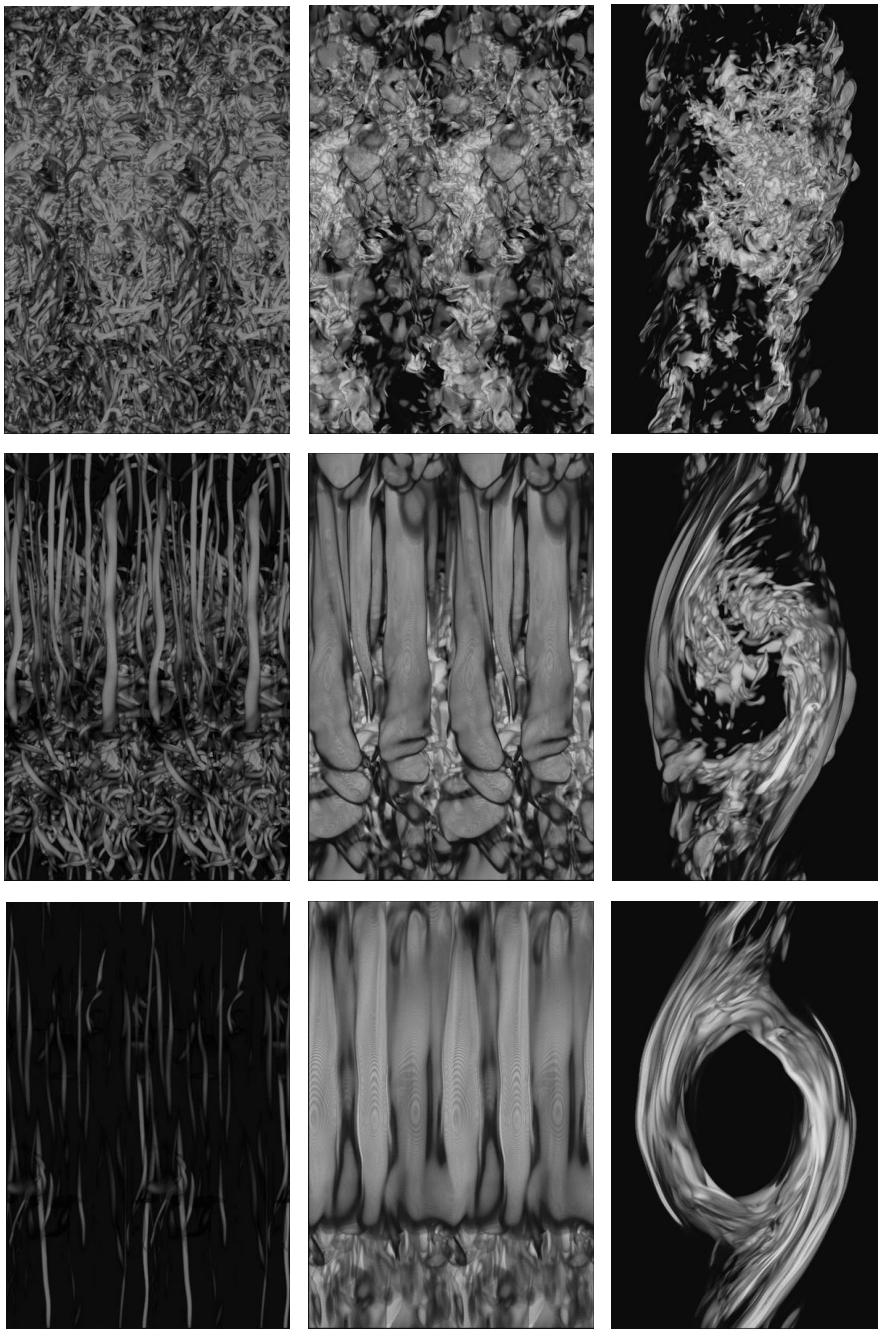

Plate 1: DNS of the Kelvin-Helmholtz instability. Bottom (middle) row shows thermal χ and viscous ε dissipation viewed from the side (above) at $t = 77$, 103, and 164. The top row depicts vortex tubes viewed from above.

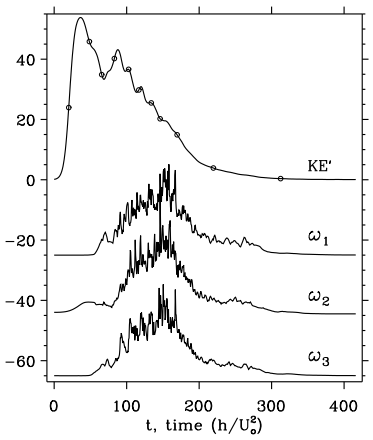

FIGURE 1. Billow and fluctuation kinetic energy (KE) and max(ω_i) versus time. ω_1 (ω_2) [ω_3] has been shifted down by 25 (45) [65].

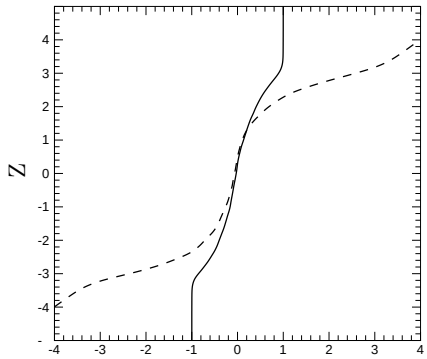

FIGURE 2. Mean velocity (——) and temperature (- - -) profiles.

the middle, and, as a result, the motion in the edge regions is more effectively damped than in the layer interior.

2.3. *Flow decomposition and averaging procedure*

For purposes of analysis we follow Palmer *et al.* (1996) and decompose the flow fields, e.g., θ, into mean $\overline{\theta}$, residual spanwise average $\tilde{\theta}$, and fluctuating components θ': $\theta = \overline{\theta} + \tilde{\theta} + \theta'$. We identify horizontal averages, e.g., $\overline{\theta}$, with the mean field and residual spanwise averages, e.g., $\tilde{\theta}$, with the primary Kelvin vortex. Both $\overline{\theta}$ and $\tilde{\theta}$ contribute to the background environment of θ', and in what follows we lump these together into what we will refer to as the 'background field', which we denote with upper-case symbols. To simplify our notation, we will drop the use of primes for the 'fluctuating' fields, denoting them by lower-case symbols; hence, $\overline{\theta} + \tilde{\theta} = \Theta$ and $\theta' \to \theta$.

3. Statistical analysis: mathematical framework

The mathematical framework for the analysis in section4 and section 5 is developed here.

3.1. *Turbulence transport equations*

The budgets for the equations governing the evolution of the Reynolds stress, heat flux and temperature variance are given by

$$\frac{D\overline{u_i u_j}}{Dt} = \underbrace{-\left(\overline{u_j u_k}\partial_k U_i + \overline{u_i u_k}\partial_k U_j\right)}_{P_{ij}} + \underbrace{\left(Ri_i\,\overline{u_j\theta} + Ri_j\,\overline{u_i\theta}\right)}_{G_{ij}} - \underbrace{2Re^{-1}\overline{\partial_k u_i \partial_k u_j}}_{\varepsilon_{ij}} + \underbrace{\overline{p\left(\partial_j u_i + \partial_i u_j\right)}}_{\phi_{ij}} + \mathcal{D}_{ij} \tag{3.1}$$

$$\frac{D\overline{u_i\theta}}{Dt} = \underbrace{-\left(\overline{u_k\theta}\partial_k U_i + \overline{u_k u_i}\partial_k \Theta\right)}_{P_{i\theta}} - \underbrace{\left(Pe^{-1} + Re^{-1}\right)\overline{\partial_k u_i \partial_k \theta}}_{\varepsilon_{i\theta}} - \overline{p\partial_i\theta} + Ri_i\,\overline{\theta^2} + \mathcal{D}_{i\theta} \tag{3.2}$$

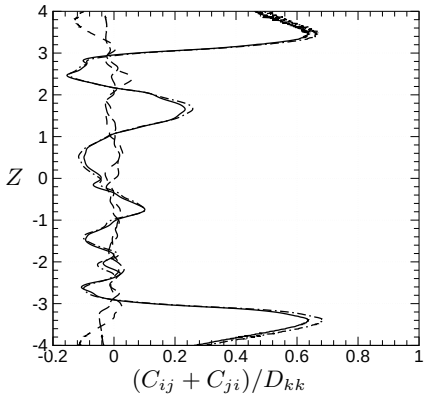

FIGURE 3. Normalized $C_{ij}+C_{ji}$; – – i=j=1; – · – i=j=2; —— i=j=3; - - - i=1, j=3.

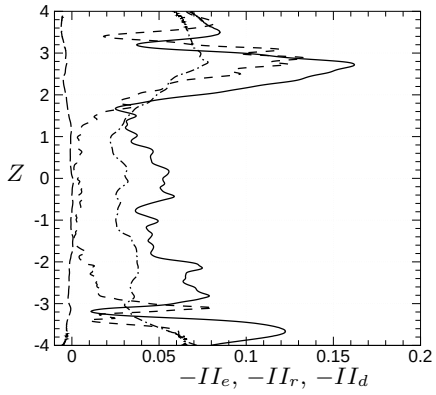

FIGURE 4. Invariants of $\overline{u_iu_j}$, ε_{ij}, and D_{ij}; - - - $(-II_e)$; —— $(-II_r)$; – · – $(-II_d)$; – – III_d.

$$\frac{D\overline{\theta^2}}{Dt} = \underbrace{-2\overline{u_k\theta}\partial_k\Theta}_{P_{\theta\theta}} \underbrace{-2Pe^{-1}\overline{\partial_k\theta\partial_k\theta}}_{\varepsilon_{\theta\theta}} + \mathcal{D}_{\theta\theta} \tag{3.3}$$

respectively, where $D/Dt \equiv \partial_t + U_k\,\partial_k$ is the total rate of change and $\mathcal{D}_{ij}$, $\mathcal{D}_{i\theta}$ and $\mathcal{D}_{\theta\theta}$ denote diffusion terms.

3.2. *Structure-based tensors*

The components of the single-point Reynolds-stress tensor $\overline{u_iu_j}$ describe the 'componentality' of the turbulence field, i.e., the strengths of different fluctuating velocity components. This, however, is insufficient to completely quantify the state of turbulence because structural information characterizing flow morphology is absent from $\overline{u_iu_j}$. It is straightforward to describe such information with two-point or spectral descriptions; however, because of their inherent complexity, such approaches are currently impractical for predictive modeling efforts. Kassinos *et al.* (2001) point out that an adequate one-point description may be possible by utilizing the so-called structure-based tensors. These are second- and third-rank tensors derived from correlations of gradients of a turbulence vector streamfunction Ψ_i: $\nabla^2\Psi_i = -\omega_i$, where ω_i is the fluctuating vorticity. The velocity is simply $u_i = \epsilon_{ijk}\partial_j\Psi_k$, and continuity imposes the free condition $\partial_k\Psi_k = 0$.

Using Ψ_i, Kassinos *et al.* (2001) introduce the following set of single-point tensors: $D_{ij} \equiv \overline{\partial_i\Psi_k\partial_j\Psi_k}$ (Dimensionality); $F_{ij} \equiv \overline{\partial_k\Psi_i\partial_k\Psi_j}$ (Circulicity); $C_{ij} \equiv \overline{\partial_k\Psi_i\partial_j\Psi_k}$ (Inhomogeneity); and $Q_{ijk} \equiv -\overline{u_j\partial_k\Psi_i}$ (Stropholysis). These tensors characterize the large-scale turbulence field. Together with $\overline{u_iu_j}$ they form a minimal tensorial base for a complete single-point turbulence theory. Members of the subset $\overline{u_iu_j}$, D_{ij}, F_{ij}, and C_{ij} are linearly independent and can be related to the trace of $\overline{u_iu_j}$ through $\overline{u_iu_j} + D_{ij} + F_{ij} - (C_{ij}+C_{ji}) = \overline{u_ku_k}\delta_{ij}$.

The information content of the individual tensors is most easily understood by considering the special case of homogeneous turbulence. Here we just mention the highlights: see Kassinos *et al.* (2001) for details.

The dimensionality tensor D_{ij} describes the anisotropy of wave-vectors in spectral space, i.e., it contains information that is distinct from that in $\overline{u_iu_j}$; if, e.g., $D_{11} = 0$, then the large-scale turbulence field is independent of the streamwise direction x. The

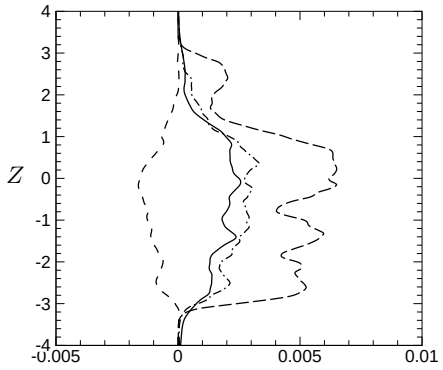

FIGURE 5. Unnormalized $\overline{u_i u_j}$; $- - -$ $\overline{u^2}$; $- \cdot -$ $\overline{v^2}$; —— $\overline{w^2}$; - - - $\overline{uw}$.

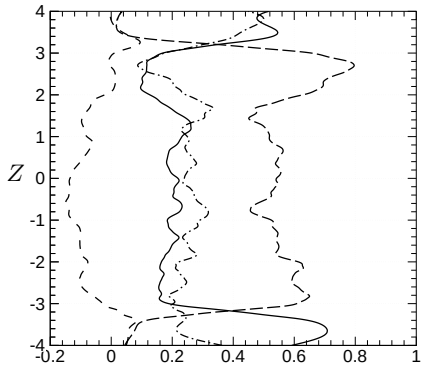

FIGURE 6. Normalized $\overline{u_i u_j}$; $- - -$ $\overline{u^2}/\overline{u_k u_k}$; $- \cdot -$ $\overline{v^2}/\overline{u_k u_k}$; —— $\overline{w^2}/\overline{u_k u_k}$; - - - $\overline{uw}/\overline{u_k u_k}$.

inhomogeneity tensor C_{ij} is a measure of departure from local homogeneity. For homogeneous turbulence, $C_{ij} \equiv 0$. The circulicity tensor F_{ij} describes the large-scale vorticity field. If one of the diagonal components dominates the others, then the largest turbulence scales create rotation predominantly about that direction. Finally, the third-rank stropholysis tensor Q_{ijk} contains information that is distinct from the other structure tensors. It relates to the pressure-strain correlation ϕ_{ij} appearing in (3.1) and is of particular importance in situations where there are significant contributions from mean or frame rotations.

4. Dynamics in the near-edge region

4.1. *Shear-layer-interior homogeneity*

We begin by examining the flow inhomogeneity $C_{ij} + C_{ji}$ during turbulence decay and restratification in figure 3. Here we see from $C_{11}/D_{kk} \approx 0$ that the flow is nearly homogeneous in the streamwise direction across the layer, justifying the streamwise-averaging procedure we have adopted. The two other diagonal components, C_{22}/D_{kk} and C_{33}/D_{kk}, are also nearly zero in the core region, indicating local homogeneity in these directions as well when $|z| < 3$.

4.2. *Edge-region flux suppression*

Figure 5 shows the shear-stress components for the same time shown in figure 3. Note the reduction in the fluctuation KE near the edges of the layer where density stratification is elevated (*cf.* figure 2). Note also the significant asymmetry that has appeared between the upper and lower edges due to the relatively larger density stratification which has developed spontaneously in the upper edge region. Animations reveal that this asymmetry results when reminants of the primary KH billow descend (by random advection), increasing the turbulence intensity of the lower edge relative to the upper edge and triggering the early collapse and restratification of the upper edge.

The enhanced stratification in the upper edge leads to the development of a significant region of flux suppression (see $\overline{uw}$ for $z > 2$ in figures 5 and 6), with flux reversal being observed momentarily. Much of the discussion that follows concentrates on the nature

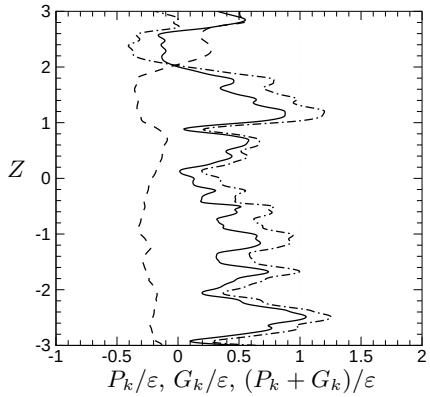

FIGURE 7. Production/dissipation rate ratio; $-\cdot- P_k/\varepsilon$; - - - G_k/ε. —— $(P_k+G_k)/\varepsilon$.

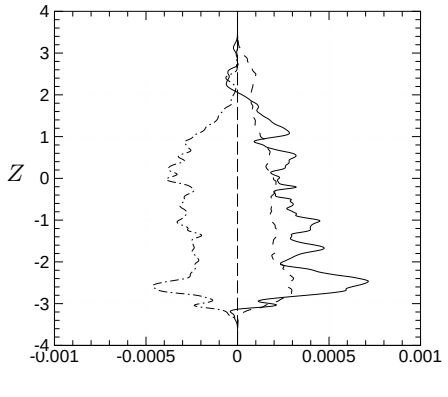

FIGURE 8. Incomplete budget for $\overline{uu}$; $-\ -\ G_{11}$; $-\cdot- \phi_{11}$; —— P_{11}; - - - ε_{11}.

and consequences of the edge-region flux reduction as a case study in the impact of stratification. We will extend this analysis in future work to examine the behavior at earlier time and for varied Ri and Re.

4.3. *Turbulence production and mean-field evolution*

As a result of the more rapid restratification near the upper edge of the shear layer, the background Richardson number is higher here and the turbulence kinetic energy is reduced. We see from the turbulence-kinetic-energy production terms

$$\mathcal{P}_k = P_k + G_k \approx \underbrace{-\overline{uw}\partial_3 U}_{\frac{1}{2}P_{11}} + \underbrace{Ri\,\overline{w\theta}}_{\frac{1}{2}G_{33}}, \tag{4.1}$$

which we obtain from the trace of (3.1), that reduction in turbulence kinetic energy is intimately tied to flux suppression. We also note that the shear production term P_k is normally positive, and the buoyancy production term $G_k = Ri\,\overline{w\theta}$ usually acts to enhance the background temperature field Θ at the expense of the turbulence. This is the behavior near midlayer. However, when flux reversal occurs, as it does for a period of time near the upper edge of the layer, the terms exchange roles, with buoyancy acting as a source in the $\overline{w^2}$ equation and shear behaving as a sink for $\overline{u^2}$. Figure 7 shows the relative contributions of P_k and G_k for kinetic energy production, demonstrating that, despite the exchange in roles for the two terms during flux reversal, shear consistently dominates buoyancy effects throughout the layer; i.e., $|P_k| > |G_k|$. The shift in the turbulence kinetic energy production from P_{11} in $\overline{u^2}$ to G_{33} in $\overline{w^2}$ has interesting consequences for stably-stratified shear-flow dynamics when flux suppression and reversal occur. First, when $P_{11} \lesssim 0$, energy transfer from the background flow is abruptly shut off; see figure 8. Secondly and perhaps more interestingly, the intercomponent energy transfer in (3.1) between $\overline{u^2}$, $\overline{v^2}$, and $\overline{w^2}$ (via pressure-strain correlations ϕ_{ij}) is fundamentally different from homogeneous shear flow. Figure 9 demonstrates this by showing the normal components of ϕ_{ij}. The majority of the layer exhibits $\phi_{11} < 0$ and $\phi_{22}, \phi_{33} > 0$, consistent with homogeneous shear-flow dynamics; however the upper edge region, where flux reversal is occuring, exhibits a change in sign of the vertical component, with the other two components retaining their midlayer signs; i.e. $\phi_{11} < 0$, $\phi_{22} > 0$, and $\phi_{33} < 0$. The peculiarity of this

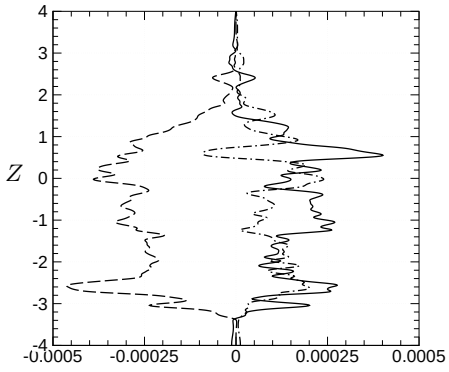

FIGURE 9. ϕ_{ij}; $---$ ϕ_{11}; $-\cdot-$ ϕ_{22}; —— ϕ_{33}

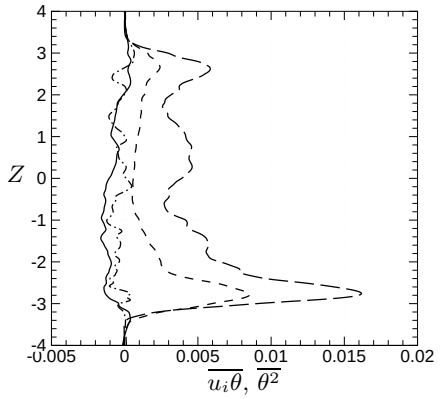

FIGURE 10. $\overline{\theta^2}$ and $\overline{u_i\theta}$; $-\ -$ $\overline{u\theta}$; $-\cdot-$ $\overline{v\theta}$; —— $\overline{w\theta}$; - - - $\overline{\theta^2}/10$.

behavior is not that ϕ_{33} has changed sign, but rather that ϕ_{11} has not. To understand the ramifications, consider the case of homogeneous shear flow unaffected by body forcing. In this case $P_{11} > 0$ and $P_{22} = P_{33} = 0$, and $\phi_{11} < 0$, $\phi_{22}, \phi_{33} > 0$. Background-flow energy is thus transferred directly to the streamwise stress componen,t and orthogonal components are subsequently fed via pressure-strain correlations. In contrast, for the case near the upper portion of the shear layer presented in figures 8 and 9, pressure-strain correlations redistribute energy into $\overline{v^2}$ from both $\overline{u^2}$ and $\overline{w^2}$, despite the fact that $P_{11} + G_{11}$ is negative. The importance of this result is that pressure-strain models employed by traditional RANS closures fail in this situation because they cannot predict $\mathrm{sign}(P_{ij} + G_{ij}) = \mathrm{sign}(\phi_{ij})$. This is similar to the blocking effect in turbulent boundary layers, except in that case wall-normal- and shear-stress components are affected, see e.g. Durbin & Pettersson Reif (2001).

4.4. *Turbulence production and $\overline{u^2}$ damping*

An apparent oddity of the normalized Reynolds-stress components (figure 6) near the edges of the shear layer is the sharp reduction in $\overline{u^2}$ relative to $\overline{v^2}$ and $\overline{w^2}$ as the far field is approached. This is particularly striking given the well-established damping of $\overline{w^2}$ in stable stratification when background shear is not present (Thoroddsen & Van Atta (1992)). Clearly, background shear introduces a fundamental change in the dynamics.

In order to explain the reduction of $\overline{u^2}$ and demonstrate its relation to flux suppression (and possible reversal), we must examine the dominant production terms for $\overline{u^2}$, $\overline{uw}$ and $\overline{w\theta}$:

$$\mathcal{P}_{11} = P_{11} + G_{11} \approx -\overline{uw}\partial_3 U \tag{4.2}$$

$$\mathcal{P}_{13} = P_{13} + G_{13} \approx -\overline{w^2}\partial_3 U + Ri\,\overline{u\theta} \tag{4.3}$$

$$\mathcal{P}_{3\theta} = P_{3\theta} + Ri\,\overline{\theta^2} \approx -\overline{w^2}\partial_3 \Theta + Ri\,\overline{\theta^2}. \tag{4.4}$$

We see that it is also instructive to consider the generation terms for $\overline{u\theta}$, $\overline{\theta^2}$, and $\overline{w^2}$:

$$P_{1\theta} \approx -\overline{w\theta}\partial_3 U - \overline{uw}\partial_3\Theta, \quad P_{\theta\theta} = -2\overline{w\theta}\partial_3\Theta, \quad \mathcal{P}_{33} = P_{33} + G_{33} \approx Ri\,\overline{w\theta}. \tag{4.5}$$

From (4.3) we see that $\overline{u\theta}$ and a reduction in $\overline{w^2}$ will act to reduce $-\overline{uw}$, which in turn through (4.2) will decrease $\overline{u^2}$. As $-\overline{uw}$ decreases, the background shear generation of

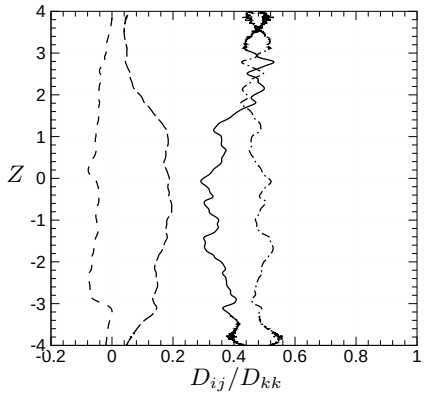

FIGURE 11. Normalized D_{ij}; $-\ -$ i=j=1; $-\cdot-$ i=j=2; —— i=j=3; - - - i=1, j=3.

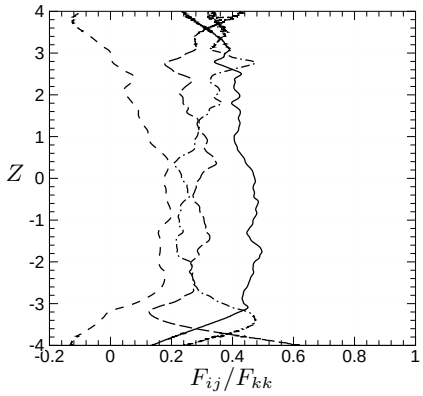

FIGURE 12. Normalized F_{ij}; $-\ -$ i=j=1; $-\cdot-$ i=j=2; —— i=j=3; - - - i=1, j=3.

turbulence kinetic energy is reduced, and therefore so is $\overline{w^2}$. It is important to note however that a change in sign of $\overline{uw}$ does *not* promote high positive levels of $\overline{u\theta}$ due to the second term $P_{1\theta}$ (4.5), suggesting that high levels of $\overline{u\theta}$ alone cannot be responsible for flux reversal when it occurs. Nevertheless, from $P_{1\theta}$ (4.5) we see that for fixed or slowly-varying values of $-\overline{w\theta}$ and $-\overline{uw}$, increases in the background gradients do result in elevated values of $\overline{u\theta}$, which can participate in reducing $-\overline{uw}$ and $\overline{u^2}$.

Similarly we can understand the suppression (and possible reversal) of $\overline{w\theta}$ by noting that for relatively fixed values of $-\overline{w\theta}$ an elevated value of $\partial_3\Theta$ will result in enhanced $\overline{\theta^2}$, which combined with a reduction in $\overline{w^2}$ will reduce $-\overline{w\theta}$ via (4.4). But, as can be seen from $P_{\theta\theta}$ (4.5), and similar to the case for $-\overline{uw}$, reduced $-\overline{w\theta}$ acts to decrease $\overline{\theta^2}$, suggesting that high levels of $\overline{\theta^2}$ alone cannot be responsible for a reversal in $-\overline{w\theta}$ when it occurs. This suggests that a reduction in $\overline{w^2}$ is the most important instigator for flux reversals, both $\overline{w\theta}$ and $\overline{uw}$.

5. Anisotropies and large-scale structures

The second invariant $II_x = -\frac{1}{2}x_{ij}x_{ij}$ of a second-rank tensor x_{ij} quantifies the departure from isotropy ($II_x = 0$). In particular $x_{ij} + \delta_{ij}/3 = \overline{u_iu_j}/\overline{u_ku_k}$ (II_r), D_{ij}/D_{kk} (II_d), and $\varepsilon_{ij}/\varepsilon_{kk}$ (II_e) reflect the character of the large ($\overline{u_iu_j}$, D_{ij}) and dissipative (ε_{ij}) scales, respectively. The profiles displayed in figure 4 reveal that the small-scale anisotropy can be comparable to, or even larger than, the integral-scale anisotropy in the strongly inhomogeneous edges of the shear layer, whereas the small-scale motion is significantly more isotropic near mid-layer. D_{ij} is less anisotropic than $\overline{u_iu_j}$ throughout the layer, and $III_d = \frac{1}{3}x_{ij}x_{jk}x_{ki} < 0$ indicates cigar-shaped features near the layer edges.

By examining the individual components of $\overline{u_iu_j}$, D_{ij}, and F_{ij} (figures 6–12), we can gain further insight into the large-scale turbulence structures (Kassinos *et al.* (2001)). For example, in the upper near-edge region with $D_{22} \approx D_{33}$ and $D_{11} \approx D_{22}/6$, we anticipate that the cigar-shaped features are aligned in the streamwise direction, are roughly six times longer in the x direction than in the other directions, and since $\overline{u^2} >> \overline{v^2} \approx \overline{w^2}$, these features are strongly 'jetal' in character. At mid-layer the diagonal components of D_{ij} are roughly in the ratio $(D_{11} : D_{22} : D_{33}) \approx (2 : 5 : 3.4)$ and we expect less elongated structures here, extending roughly 2.5 times in the streamwise direction as in

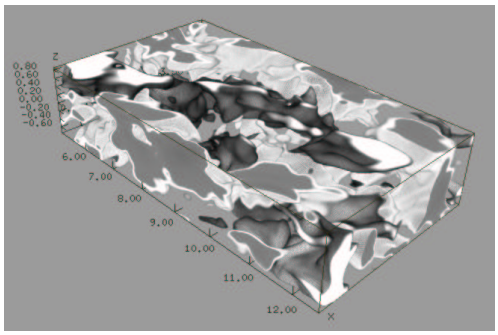

FIGURE 13. Streamwise fluctuations in the center of the layer. Dark (light) regions with light (dark) cores represent $u > 0$ ($u < 0$).

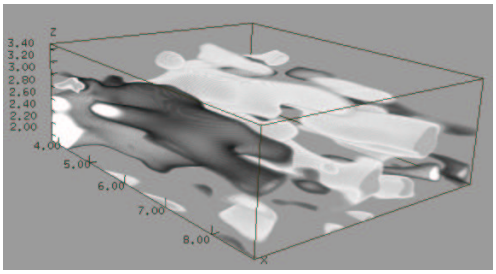

FIGURE 14. Streamwise fluctuations at the edge of the layer. Dark (light) regions with light (dark) cores represent $u > 0$ ($u < 0$).

the spanwise, and possessing $\sim 30\%$ greater height than spanwise extent. Figures 13 and 14 support these expectations. In particular, note the nearly circular (spanwise-flattened) $y-z$ cross-sections of features at the $x = 12.56$ ($x = 9.0$) cutting plane in the upper-edge (mid-layer) region.

The circulicity tensor (figure 12), which quantifies large-scale turbulence circulation, exhibits a tendency for large-scale vertical vorticity at mid-layer with $F_{33} > F_{11} \gtrsim F_{22}$. This results from jetal motions in the horizontal plane and is identical to the behavior in the unstratified case (Kassinos *et al.* (2001)). Near the edges of the layer F_{11} decreases while F_{22} grows until $F_{22} \approx F_{33}$, and just outside the layer F_{22} surpasses F_{33} to become the dominant circulation direction. This behavior results from the strong vortex sheet adjacent to the turbulent layer which acts as the transition interface between turbulent and irrotational flow.

6. Conclusions

We have presented Reynolds-stress and heat-flux budgets for stratified shear flow during layer restratification. During this time the outer regions of the shear layer exhibit flux suppression and reversal, both for $\overline{uw}$ and $\overline{w\theta}$; we offer an explanation for this behavior. The reversals are most pronounced at the top of the layer where turbulence kinetic energy is severely damped by the action of stable stratification.

We also examined the ability of single-point structure tensors to describe the features exhibited by 3D volume-rendered depictions of the flow. The structure tensors appear to capture and quantify the relevant flow morphology.

We will extend this analysis to earlier times and different Re and Ri so we can evaluate the robustness of the result. Furthermore, because the edges of the shear layer appear to pose important challenges for modeling, it is imperative that we insure that quantification of the edge regions is reliable. For this reason future characterization will adopt the conditional-sampling technique of Bisset *et al.* (2002).

Acknowledgment

The authors acknowledge discussions with Professors P. A. Durbin, J. H. Ferziger and J. C. R. Hunt, and with Drs F. Jacobitz, S. C. Kassinos, N. N. Mansour and M. M. Rogers. Plate 1 was created using OGLE, a 3D visualization package written by Dr. Michael

Gourlay. Figures 13 and 14 were created using Viz, a volume-rendering tool maintained at the Norwegian Defence Research Establishment. JW is partially supported by AFRL F19628-02-C-0037, DOE (Environmental Meteorology Program) DE-FG03-99ER62839, and NASA NASW-99026. Simulations were conducted on Cray T3E's at the U.S. Army Engineer Research Development Center and at the Naval Oceanographic Office as part of the DoD Airborne Laser Challenge program.

REFERENCES

Bisset, D. K., Hunt, J. C. R., & Rogers, M. M. 2002 The turbulent/non-turbulent interface bounding a far wake. *J. Fluid Mech.* **451**, 183–410.

Duda, R. O. & Hart, P. E. 1973 *Pattern Classification and Scene Analysis.* Wiley, New York.

Durbin, P. A. & Pettersson Reif, B. A. 2001 *Statistical Theory and Modeling for Turbulent Flows.* Wiley, New York.

Fritts, D. C., Arendt, S. & Andreassen, Ø. 1998 Vorticity dynamics in a breaking internal gravity wave, 2. Vortex interactions and transition to turbulence. *J. Fluid Mech.* **367**, 47–65.

Jang, P. S., Benney, D. J. & Gran, R. L. 1986 On the origin of streamwise vortices in a turbulent boundary layer. *J. Fluid Mech.* **169**, 109–123.

Jeong, J. & Hussain, F. 1995 On the identification of a vortex. *J. Fluid Mech.* **285**, 69–94.

Kassinos, S. C., Reynolds, W. C. & Rogers, M. M. 2001 One-point turbulence structure tensors. *J. Fluid Mech.* **428**, 213–248.

Klaassen, G. P. & Peltier, W. R. 1985 The onset of turbulence in finite-amplitude Kelvin-Helmholtz billows. *J. Fluid Mech.* **155**, 1–35.

Klaassen, G. P. & Peltier, W. R. 1991 The influence of stratification on secondary instability in free shear layers. *J. Fluid Mech.* **227**, 71–106.

Miles, J. W. 1960 On the stability of heterogeneous shear flows. *J. Fluid Mech.* **10**, 496–508.

Palmer, T. L., Fritts, D. C., Andreassen, Ø. & Lie, I. 1994 Three-dimensional evolution of Kelvin-Helmholtz billows in stratified compressible flow. *Geophys. Res. Letters* **21**, 2287–2290.

Palmer, T. L., Fritts, D. C. & Andreassen, Ø. 1996 Evolution and breakdown of Kelvin-Helmholtz billows in stratified compressible flows, II: Instability structure, evolution and energetics. *J. Atmos. Sci.* **53**, 3192–3212.

Smyth, W. D. & Moum, J. N. 2000a Length scales of turbulence in stably stratified mixing layers. *Phys. Fluids* **12**, 1327–1342.

Smyth, W. D. & Moum, J. N. 2000b Anisotropy of turbulence in stably stratified mixing layers. *Phys. Fluids* **12**, 1343–1362.

Spalart, P. R., Moser, R. D. & Rogers, M. M. 1991 Spectral methods for the Navier-Stokes equations with one infinite and two periodic directions. *J. Comput. Phys.* **96**, 297–324.

Thoroddsen, S. & Van Atta, C. W. 1992 The influence of stable stratification on small-scale anisotropy and dissipation in turbulence *J. Geophys. Res.* **97**, 3647–3658.

Werne, J. & Fritts, D. C. 1999 Stratified shear turbulence: evolution and statistics. *Geophys. Res. Letters* **26**, 439–442.